JOURNAL OF MATERIALS SCIENCE **38** (2003) 35–49

A three dimensional model for direct laser metal powder deposition and rapid prototyping

M. LABUDOVIC
Corning Lasertron, R & D, 11 Oak Park, M/S LZ-727, Bedford, MA 01730, USA
E-mail: marko_L@email.msn.com

D. HU, R. KOVACEVIC
Department of Mechanical Engineering, Southern Methodist University, P.O. Box 750337, Dallas, Texas, USA

A three-dimensional model for direct laser metal powder deposition process and rapid prototyping is developed. Both numerical and analytical models are addressed. In the case of numerical modeling, the capabilities of ANSYS parametric design language were employed. The model calculates transient temperature profiles, dimensions of the fusion zone and residual stresses. Model simulations are compared with experimental results acquired on line using an ultra-high shutter speed camera which is able to acquire well-contrasted images of the molten pool, and off-line using metallographical and x-ray diffraction analyses. The experiments showed good agreement with the modeling. The results are discussed to provide suggestions for feedback control and reduction of residual stresses.

Nomenclature

A	Heat absorptivity of laser beam on metal surface
C	Specific heat (J/kg · K)
d	Diameter of the laser beam (m)
d_z, d_x	Length (width) of the laser beam in z (x) direction (m)
I	Thermal flux density of laser beam (J/s · m^2)
E	Elastic modulus (N/mm^2)
h	Heat transfer coefficient (W/m^{2}K)
H	Enthalpy (J/kg)
$H(.)$	Heaviside function (unit step function)
k	Boltzmann's constant ($K = 1.38066 \times 10^{-23}$ Ws/K)
K	Heat conductivity (J/m · s · K)
L_f	Latent heat of fusion (J/kg)
P	Laser beam power (J/s)
$\mathbf{P}$	Surface pressure vector (N/m^2)
$\dot{q}$	Rate of heat generation (J/s · m^3)
$\dot{q}_{ii}$	Tensor of heat flow derivatives (J/mm^{3}s)
$\dot{Q}_v$	Volume-specific heat flow or source density (J/mm^{3}s)
$\mathbf{Q}$	Body force vector (N/m^3)
r	Distance from the center of the laser beam (m)
r_b	Effective laser beam radius (m)
S	Area (m^2)
S_{sl}	Area of the solid-liquid interface (m)
t	Time (s)
T	Temperature (K)
$\dot{T}$	Cooling rate (K/s)
u, v, w	Displacement components in the x, y, z directions, respectively (m)
$\mathbf{u}$	Displacement vector (m)
V	Volume (m^3)
y_m	Molten pool depth (m)
Δt	Incremental time (s)
α	Thermal expansion coefficient (1/K)
ρ	Density (kg/m^3)
ν	Poisson's ratio
ε	Emissivity
$\delta(.)$	Dirac delta function
ε	Strain tensor in updated Lagrange configuration
$\dot{\varepsilon}_{ii}$	Tensor of elastic volumetric strain rates (1/s)
$\dot{\varepsilon}_{vpij}$	Tensor of viscoplastic strain rates (1/s)
ξ	Inelastic heat fraction
σ	Stefan-Boltzmann constant ($\sigma = 5.670 \times 10^{-8}$ W/m^2 K^4 σ)
σ_{dij}	Deviatoric stress tensor (N/mm^2)
σ	Stress tensor in updated Lagrange configuration (N/m^2)
ξ, ζ, χ	Local coordinates

1. Introduction

The direct laser metal powder deposition process is laser-assisted, direct metal manufacturing process for rapid prototyping under development at Southern Methodist University. The process is similar to the laser-engineered net shaping (LENS)^{TM} process developed at Sandia National Laboratories [1]. It incorporates features from stereolithography and laser cladding, that use computer-aided design (CAD) file cross sections (stl file) to control the forming process. Metal-powder particles are delivered in an argon gas stream into the focus of the laser beam to form a molten

pool. The part is then driven by an xy positioning system to generate a three-dimensional part by layer-wise, additive processing.

In order to understand the thermal behavior of the process, an on-line high-shutter speed imaging was coupled with a microstructural analysis, x-ray analysis, analytical and numerical modeling. Since the thermal behavior controls the morphology and properties of the specimen; thermal measurements, microstructural analysis, and modeling can be combined to develop the process parameters to control the microstructural development and tailor the properties of the specimens. As a first step, a high-shutter speed imaging is employed in monitoring the deposition of 100 mesh MONEL 400-alloy powder on AISI 1006 steel plate, at a variety of laser powers and scanning speeds. The microstructure of the deposits was investigated, and the dimensions of the fusion zone were correlated to the thermal conditions at solidification. Finally, both analytical and numerical models were developed to determine the thermal history of the specimens both in the areas that are accessible or not accessible to high-shutter speed imaging measurements. The results from heat transfer analysis were then used as loads for finite element analysis of residual stresses. Residual stresses were investigated with an x-ray diffraction technique, and the results were correlated with those obtained by the finite element modeling.

2. The Physical description of the phenomena

Since direct laser powder deposition is a thermal process, the well-known heat conduction equation plays a central role in the physical modeling of the process. The heat conduction equation follows from the energy balance of an appropriately chosen volume and consists of the diffusive heat flows, the convective heat flows, and the possible sources of heat [2].

For the thermo-mechanical coupled system, the thermal equilibrium equation for analysis of heat transfer in a domain D can be written as:

$$k\left(\frac{\partial^2 T}{\partial x^2}+\frac{\partial^2 T}{\partial y^2}+\frac{\partial^2 T}{\partial z^2}\right)+\dot{q}=\rho c\dot{T}+v\frac{\partial T}{\partial z} \quad (1)$$

To obtain the solution from the thermal equilibrium equation, the boundary conditions and the initial conditions are needed.

The initial condition is:

$$T(x,y,z,0)=T_0 \quad \text{for} \quad (x,y,z)\in D. \quad (2)$$

The essential boundary condition is:

$$T(x,0,z)=T_0 \quad (3)$$

on the boundary S_1 for $(x,z)\in S_1$ and $t>0$. S_1 represents the bottom surface of the plate. The natural boundary conditions can be defined by:

$$k_n\frac{\partial T}{\partial n}-q+h(T-T_0)+\sigma\varepsilon\left(T^4-T_0^4\right)=0 \quad (4)$$

on the boundary S_2 for $(x,y,z)\in S_2$ and $t>0$. S_2 represents those surfaces that are subjected to radiation, convection and imposed heat fluxes.

The inclusion of the temperature-dependant thermophysical and mechanical properties, and a radiation term in the above boundary condition makes this type of analysis highly nonlinear. Since the incorporation of radiation effects are found to increase the solution time by as much as three times, an empirical relationship as proposed by Vinokurov [3] was used:

$$H=2.4\times10^{-3}\varepsilon T^{1.61} \quad (5)$$

Equation 5 combines the effect of radiation and convection into a "lumped" heat transfer coefficient. The associated loss in accuracy using this relationship is estimated to be less than 5% [3].

The fundamental equation of thermomechanics of elastic-viscoplastic continua follows according to [4]:

$$c_\rho\dot{T}+\dot{q}_{ii}=\dot{Q}_v-\frac{E_\alpha T}{1-2v}\dot{\varepsilon}_{ii}+\xi\sigma_{dij}\dot{\varepsilon}_{vpij} \quad (6)$$

where ξ is the inelastic heat fraction; $\xi\le1.0$, allows for the fact that all inelastic deformation energy is dissipated in the heat, but that part of it may appear in the microstructural change.

The restriction to the plastic behavior without viscosity is adequate for the majority of laser surface treatment residual stress problems [4]. Therefore, the viscosity behavior in Equation 6 is neglected.

3. Simplified heat conduction equation

From the above analysis of the physical phenomena, the following assumptions can be made:

1. The work piece is initially at 298 K. Both the work piece and the coordinate mesh are fixed and the laser beam moves in the positive z-direction with a constant velocity, v.
2. All thermophysical, as well as mechanical properties, are considered to be temperature-dependent. These properties are given in [5] as well as the temperature dependent stress-strain curves used in model.
3. The laser beam diameter is defined as the diameter in which the power density is reduced from the peak value by a factor of e^2 [6].
4. During the simulation, the thermal load is given in the form of the thermal flux density, which obeys normal distribution as follows: [7]

$$I=\frac{2AP}{\pi r_b^2}\exp\left(-\frac{2r^2}{r_b^2}\right) \quad (7)$$

giving the mean thermal flux density within the area of the laser beam scanning [7]

$$I_m=\frac{1}{\pi r_b^2}\int_0^{r_b}I(2\pi r)\,\mathrm{d}r$$
$$=\frac{2\pi}{\pi r_b^2}\int_0^{r_b}\frac{2AP}{\pi r_b^2}\exp\left(-\frac{2r^2}{r_b^2}\right)r\,\mathrm{d}r=\frac{0.865AP}{\pi r_b^2} \quad (8)$$

5. The latent heat of fusion is simulated by an artificial increase in the liquid specific heat according to

Brown and Song [8] and the relationship between the enthalpy (H), density (ρ) and specific heat (c):

$$H = \int \rho c(T)\,\mathrm{d}T \tag{9}$$

6. Since the direct laser metal powder deposition involves very rapid melting and solidification, convective redistribution of heat within the molten pool is not significant (whereas it is in other processes where a liquid pool is permanent). Convective flow of heat, therefore, is neglected.

4. Solution of the heat conduction equation

4.1. The use of Green's function

A well-known approach to solve the simplified heat conduction equation (1) given its boundary and initial conditions is by the use of Green's functions [2]. Green's function, for the problem under consideration, is the analytical solution of Equations 1–4 with $I = \delta(x)\delta(y)H(t)$, where $\delta(.)$ is the Dirac delta function and $H(.)$ is the unit step function of Heaviside function. That is the Green's function $G\ (x, y, z, t, x', y', z', t', v, K, k)$ represent the temperature at (x, y, z) at time t due to a point source of unit strength generated at (x', y', z') at time t', which is moving with velocity v. By integrating the product of the Green's function G with the actual absorbed power density I_m, over the dimensions of the laser spot and time, the temperature $T\ (x, y, z, t)$, induced by the laser beam moving over the surface ($y' = 0$), is obtained:

$$T(x, y, z) = T_0 + \int_0^t \int_{-\infty}^{\infty} \int_{-\infty}^{\infty} G(x, y, z, t, x', 0, z, t', v) \times AI(x', y', t')\,\mathrm{d}x'\,\mathrm{d}y'\,\mathrm{d}t' \tag{10}$$

Unfortunately, no explicit analytical solution of Equation 10 for an arbitrary intensity profile I can be found. However, the equation can be solved in explicit from after introducing several approximations. To test validity, such an approximated analytical model was compared to the numerical solution.

4.2. Analytical solution of the model

4.2.1. Maximum surface temperature induced by stationary laser beam

For stationary ($v = 0$) laser beam, analytical models for the maximum surface temperature are available from literature, and these can be calculated from Equation 10. The maximum steady surface temperature induced by a stationary Gaussian intensity profile (TEM_{00}), with diameter d, equals [2]

$$T_0^G\{0, 0, 0) = \frac{AP_L}{dK}\sqrt{\frac{2}{\pi}} \tag{11}$$

4.2.2. Maximum surface temperature induced by fast moving laser beam

With the velocity of the laser beam approaching infinity, the heat flow in the solid can be approximated by one-dimensional flow perpendicular to the surface of the workpiece [2]. In addition, since the intensity profiles under consideration are symmetric with respect to the x-axis, then the maximum surface temperature for high laser beam velocities is reched at $z = 0$. Hence, the maximum surface temperature induced by the Gaussian intensity profile is [10]

$$T_\infty^G = \frac{4C\sqrt{2}}{K(\pi d)^{\frac{3}{2}}} AP_L\sqrt{\frac{k}{v}},\ C = \max_{x \in R} \times \left\{ \int_{-\infty}^{\chi} \frac{\exp[-2\eta^2]}{\sqrt{\chi - \eta}}\,\mathrm{d}\eta \right\} \approx 1.81 \tag{12}$$

4.2.3. Maximum surface temperature induced at intermediate velocities

By combining the solutions for the stationary T_0 and the fast moving beam T_∞, a following equation for the Gaussian intensity profile is obtained [11]

$$T_v^G = \frac{4C\sqrt{2}}{dK\sqrt{\pi}} AP_L \sqrt{\frac{k}{\pi^2 dv + (4C)^2 k}} \tag{13}$$

To evaluate the accuracy of this analytical expression, the Equation 13 is compared to the corresponding temperatures obtained by the numerical model.

4.3. Geometry of the molten pool

The geometry of the molten pool is determined by the energy balance. In the case of direct laser metal powder deposition, the energy balance consists of three terms: the absorbed laser energy Q_L, the energy Q_C transported by heat conduction from the liquid-solid interface of the molten pool into the non-molten material, and the energy Q_F required to create a molten pool (latent heat of fusion). The energy balance reads:

$$Q_L - Q_F = Q_C \tag{14}$$

4.3.1. Laser energy

The laser energy Q_L absorbed by the work piece, can be approximated by:

$$Q_L = AP_L t_i \tag{15}$$

Where t_i denotes the interaction time of the laser beam with a given point on the surface of the work piece. This interaction time is approximated by [12]

$$t_i = \frac{d}{v} \tag{16}$$

where d denotes the diameter of the laser beam.

4.3.2. Heat conduction

The energy Q_C, which flows from the molten pool into the solid material, can be calculated from the heat enclosed by the heat affected zone under consideration, and equals:

$$Q_C = \rho c_p \int_{V_s} T(x, y, z, t_i) dV_s \tag{17}$$

where V_s denotes the heat affected zone in the solid under the molten pool, and $T(x, y, z, t_i)$ denotes the corresponding temperature field at time $t = t_i$. It is assumed that the heat transfer under the molten pool may

be considered as one-dimensional. Then, according to [13]

$$T(z,t_i) = (T_m - T_0)erfc\left(\frac{y}{2\sqrt{kt_i}}\right) + T_0 \qquad (18)$$

The thickness of the heat affected zone V_s is assumed to be equal to the heat penetration depth i.e. $\delta_h = 2\sqrt{kt_i}$. Then the integral in Equation 18 can be evaluated if the area S_{sl} of the solid-liquid interface is known. Assuming the parabolic shape of the solid-liquid interface:

$$Q_C = \frac{4}{3} y_m \pi R_m \rho c_p (T_m - T_0) \int_0^{2\sqrt{kd/v}} \times \left[erfc\left(\frac{yv}{2\sqrt{kdv}}\right) + T_0\right] \mathrm{d}y \qquad (19)$$

where y_m is the depth of the molten pool, and R_m is the radius of the molten pool.

4.3.3. Latent heat of fusion

The energy Q_F, required to create a molten pool, follows from the latent heat of fusion L_f per unit mass of the material and the volume V_l of the molten pool:

$$Q_F = L_f \rho V_l \qquad (20)$$

in which the volume V_l of the molten pool can be calculated as:

$$V_l = \int_{-y_m}^{0} \pi r^2 \,\mathrm{d}y = \int_{-y_m}^{0} \pi R_m^2 \left(\frac{y}{y_m} + 1\right) \mathrm{d}y = \frac{\pi y_m R_m^2}{2} \qquad (21)$$

4.3.4. Depth of the molten pool

Substitution of Equations 15, 16, 19–21 into the energy balance equation yields:

$$y_m = \frac{2AP_L}{\rho c_p C_2 T_m \sqrt{kdv}} \qquad (22)$$

This equation shows a linear dependence of the molten pool depth on the ratio $P_L/(\sqrt{dv})$, which is sometimes referred as the specific energy [14]. Note that the similar relation holds for the maximum temperature (Equation 13).

5. Numerical solution of the model and computer algorithm

In order to analyze the movement and deformation of the configuration in finite element method (FEM), suppose that the equilibrium states at all the time steps from 0 to t have been obtained. Then, according to the virtual work principle [15], the equilibrium equation at time $t + \Delta t$ can be expressed as follows:

$$\int_V \boldsymbol{\sigma} \cdot \delta\varepsilon dV = \int_V \mathbf{q} \cdot \delta\mathbf{u} dV + \int_S \mathbf{p} \cdot \delta\mathbf{u} dS \qquad (23)$$

To account for the large deformation, the following shape functions, with extra shape functions (ESF) for element type of 8-node bricks, are used:

$$\begin{aligned} u &= \tfrac{1}{8}[\mathbf{u_I}(1-\xi)(1-\zeta)(1-\chi) \\ &\quad + \mathbf{u_J}(1+\xi)(1-\zeta)(1-\chi) \\ &\quad + \mathbf{u_K}(1+\xi)(1+\zeta)(1-\chi) \\ &\quad + \mathbf{u_L}(1-\xi)(1+\zeta)(1-\chi) \\ &\quad + \mathbf{u_M}(1-\xi)(1-\zeta)(1+\chi) \\ &\quad + \mathbf{u_N}(1+\xi)(1-\zeta)(1+\chi) \\ &\quad + \mathbf{u_O}(1+\xi)(1+\zeta)(1+\chi) \\ &\quad + \mathbf{u_P}(1-\xi)(1+\zeta)(1+\chi)] \\ &\quad + \mathbf{u_I}(1-\xi^2) + \mathbf{u}_2(1-\zeta^2) + \mathbf{u}_3(1-\chi^2) \\ v &= \tfrac{1}{8}[\mathbf{v_I}(1-\xi)\cdots \qquad \text{(analogous to } u\text{)} \\ w &= \tfrac{1}{8}[\mathbf{w_I}(1-\xi)\cdots \qquad \text{(analogous to } u\text{)} \end{aligned} \qquad (24)$$

where $\mathbf{u_I}$ (I = I, J, K, L, M, N, O, P) are nodal displacements.

Discretization of this problem is accomplished by means of the standard finite element procedure. Thus, the result of aggregation is a group of nonlinear equations. The Newton-Raphson method is used to linearize these equations:

$$[K]\{\Delta u\} = \{F^a\} - \{F_{nr}\} \qquad (25)$$

where $[K] = \int_V [B]^T [D^{ep}][B] dV$ is the tangential stiffness matrix, $[B]$ is the general geometric matrix, $[D^{ep}]$ is the elasto-plastic stress-strain matrix, $\{\Delta u\}$ is the displacement incremental at the element nodes, $\{F^a\}$ is the applied force vector, and $\{F^{nr}\} = \int_V [B]^T \{\sigma\} dV$ is Newton-Raphson restored force vector.

ANSYS provides a convenient means of numerically modeling direct laser metal powder deposition process. This requires an integration of the heat conduction equation with respect to time. In the finite element formulation, this equation can be written for each element as:

$$[C_T]\{\dot{T}\} + [K_T]\{T\} = \{Q\} \qquad (26)$$

where $[C_T][C_T] = \int_V \rho c [N][N]^T dV$ is the heat capacity matrix, $[N]$ is the shape function matrix, $[K_T] = \int_V k[B][B]^T dV$ is the heat conduction matrix, $\{T\}$ and $\{\dot{T}\}$ are nodal temperature vector and nodal temperature rate vector, respectively, and $\{Q\}$ is heat flux vector.

The moving laser beam is simulated using the ANSYS Parametric Design Language (APDL) to provide the heat boundary conditions at different positions at different times. The first iteration in the solution procedure solves the system equations at an assumed starting temperature (298 K), and subsequent iterations use temperatures from previous iterations to calculate the thermal conductivity and specific heat matrices. The first element was positioned onto the substrate with a set initial and boundary conditions. For subsequent elements, the model used the results from the previous step as the initial condition for each new element birth. This was repeated for all birthing events until the

geometry was complete. The iterative process continues for time period T until a converged solution is achieved or until the dynamic equilibrium of heat exchange is established.

A study of the heat-transfer problem allows the determination of the temperature distribution within a body. One can then determine the amount of heat moving into or out of the body, and the residual stresses. Following, the basic equation for thermo-mechanical coupled calculation is as follows:

$$\begin{bmatrix} [0] & [0] \\ [0] & [C] \end{bmatrix} \begin{Bmatrix} \{\dot{u}\} \\ \{\dot{T}\} \end{Bmatrix} + \begin{bmatrix} [K] & [0] \\ [0] & [K_T] \end{bmatrix} \begin{Bmatrix} \{u\} \\ \{T\} \end{Bmatrix} = \begin{Bmatrix} \{F\} \\ \{Q\} \end{Bmatrix} \tag{27}$$

where $\{F\}$ is the force vector including applied nodal force and the force caused by the thermal strain.

The residual stresses caused by inhomogeneous thermal expansion (or contraction) are termed "thermal stresses". Elastic thermal stresses disappear after removing the inhomogeneous temperatures by which they have been caused. For this reason, many authors do not classify them as residual stresses. Where major differences in temperature exist, the thermal stresses give rise to plastic deformations. After removal of the temperature differences, residual stresses remain. The plastic behavior is incorporated in the model by making use of the data given in [16].

ANSYS provides the performance of an Indirect Coupled-Field Analysis for implementing the above equations for calculating residual stresses. In this method, one performs two sequential analysis, using results from the first analysis as loads for the second analysis. Following, the algorithm for a residual-stress analysis is summarized in Fig. 1.

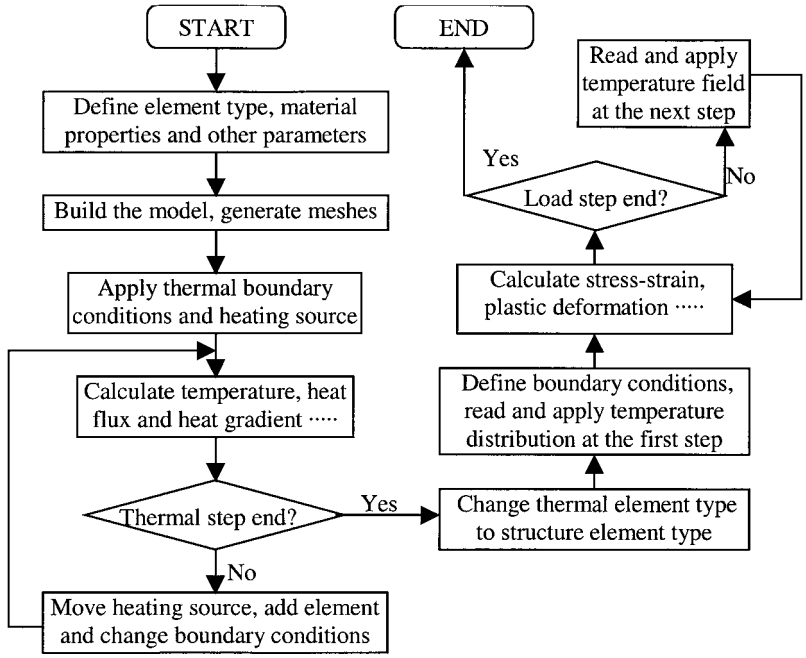

Figure 1 Computer algorithm.

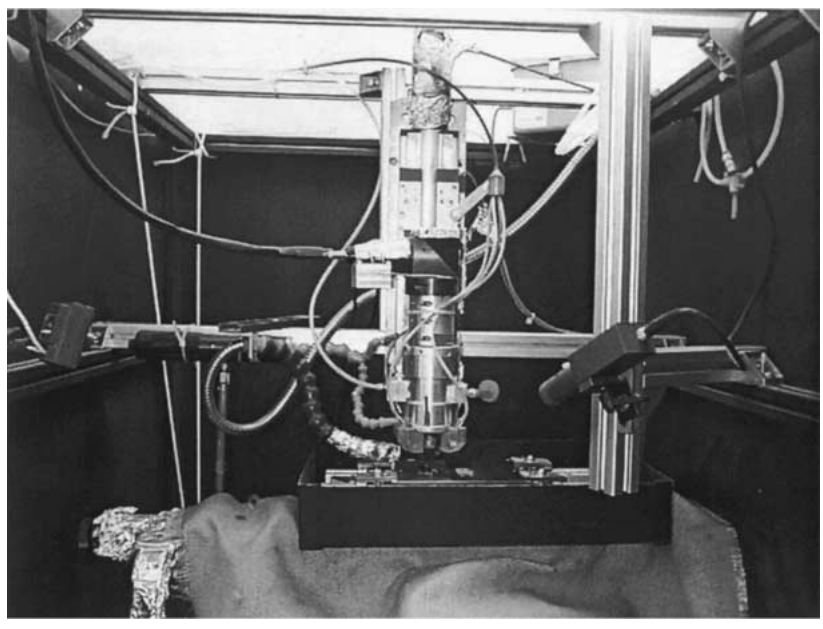

Figure 2 Experimental set-up.

6. Experiment

The experimental set-up of a Nd : YAG laser, three axis CNC positioning system, powder delivery system, laser-strobe vision system, shielding gas, and work-piece is shown in Fig. 2. The deposits were built by injecting the 100 mesh MONEL 400—alloy powder on the AISI 1006 steel plate into the Nd : YAG laser—generated molten pool. Argon was used as a shielding gas.

A fiber optic conducted a 337-nm wavelengyh laser light illuminating the Nd : YAG laser-treating area. The illuminating laser is nitrogen pulse laser with 5 ns pulse

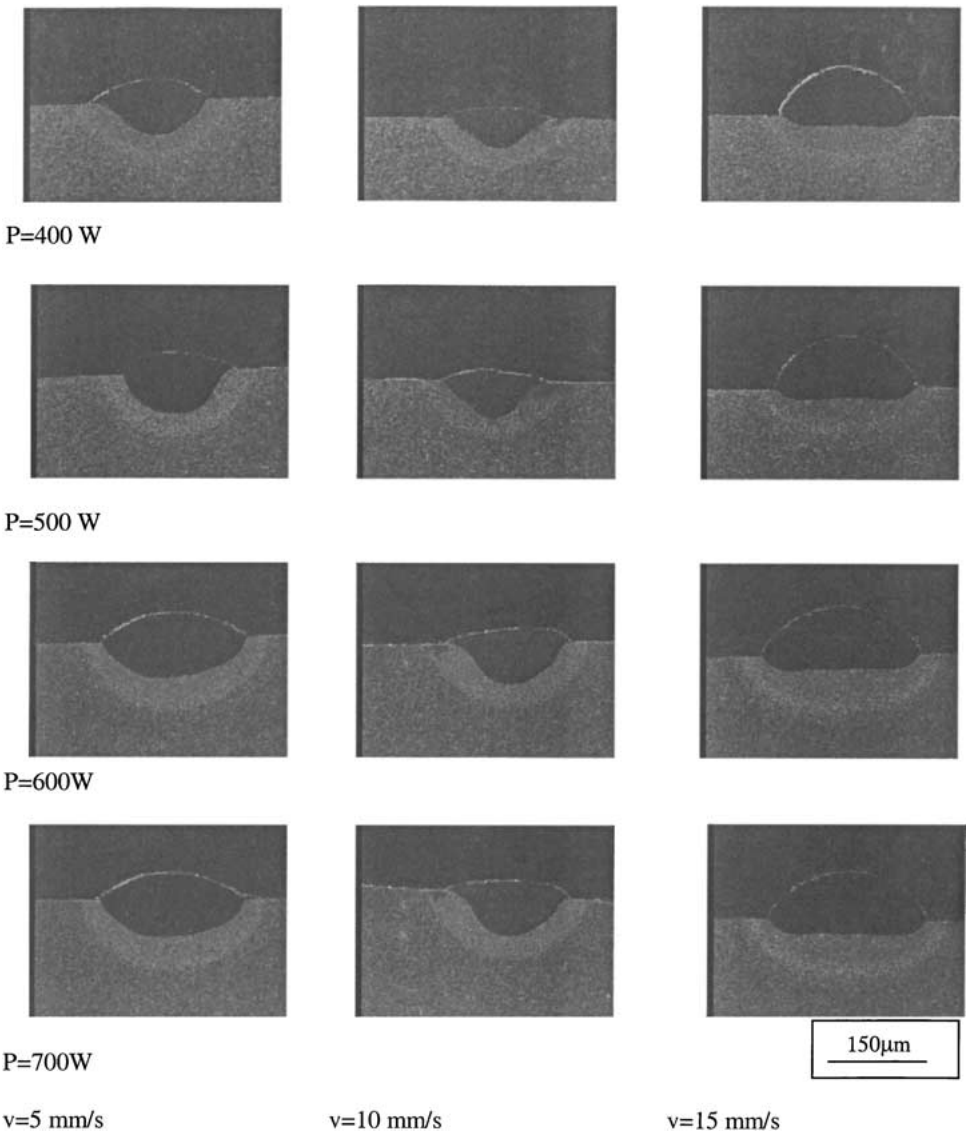

Figure 3 Macrographs showing the results of preliminary experiments of varying laser processing parameters (laser power and scanning speed).

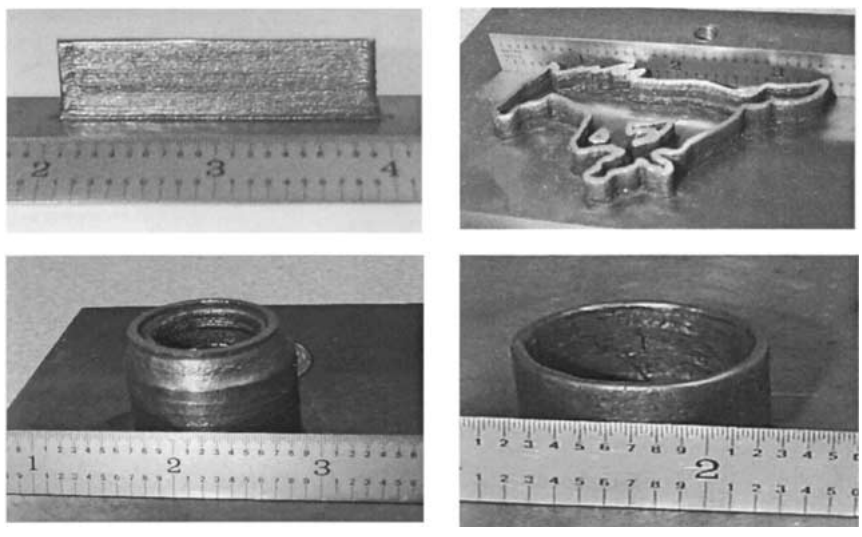

Figure 4 Parts built by direct laser metal powder deposition process.

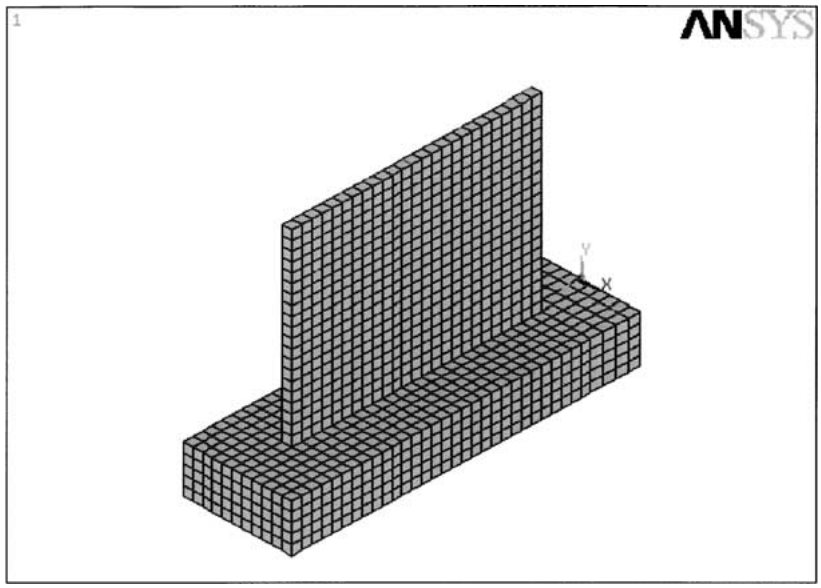

Figure 5 Finite element mesh for the ANSYS analysis.

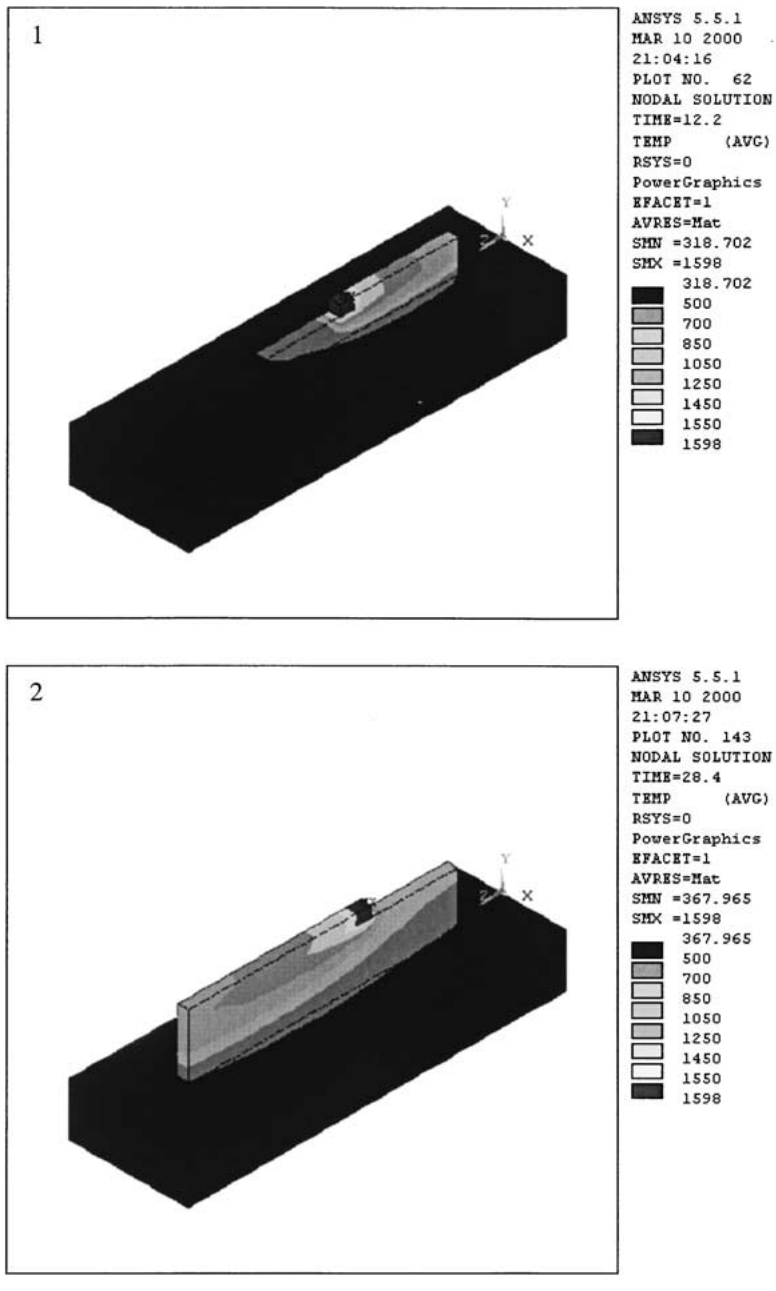

Figure 6 Temperature distribution during the direct laser metal powder deposition (laser power: 600 W, scanning speed: 10 mm/s): (1) $\tau = 12.2$ s and (2) $\tau = 28.4$ s.

duration synchronizing with the high-speed shutter of the camera. The camera of the laser strobe vision system is equipped with UV filter that only allows light near a 337 nm wavelength to pass. During the illumination period, the intensity of the illuminating laser can suppress the spatter and plasma light. Due to the reflection of the mirror-like molten pool, a well-contrasted image of the molten pool was obtained. A frame grabber installed on a PII 350 PC computer acquired images from the ultra-high shutter speed camera at 30 Hz. The image processing and recognition was completed on the same computer.

In preliminary experiments, laser-processing parameters (laser power and scanning speed) were optimized in order to achieve a good bonding of the deposited layers and satisfactory depth of penetration without excessive heat input (Fig. 3). The parts built with this experimental set-up, and after process parameter optimization, are shown in Fig. 4.

7. Modeling results and discussion

7.1. The analysis of heat transfer

The comparison of experimental with simulated results allows the estimation of the relative importance and role

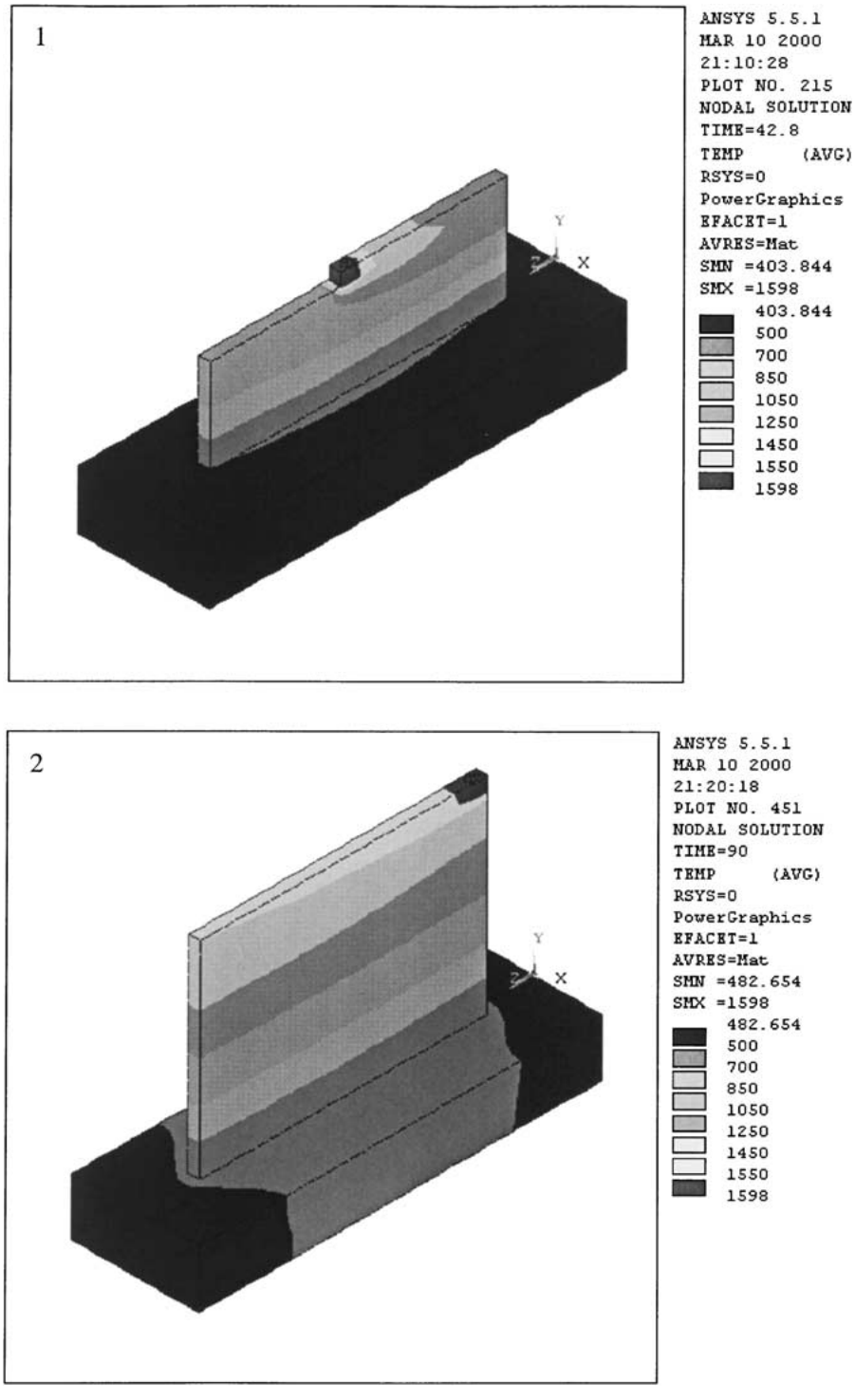

Figure 7 Temperature distribution during the direct laser metal powder deposition (laser power: 600 W, scanning speed: 10 mm/s): (1) $\tau = 42.8$ s and (2) $\tau = 90$ s.

of the complex physical interactions that govern direct laser metal powder deposition process. The comparison of experiment and simulation were done on the AISI 1006 steel plate with dimensions 50 × 20 × 10 mm. The MONEL 400-alloy powder with 100 mesh was used to build 40 mm deposits (please see Fig. 4). The finite element mesh is shown in Fig. 5. The numerical model was run for both the duration of the laser heating and for the subsequent cooling period using different powers (in the range of 300 to 1000 W) and scanning speeds (in the range of 5 to 15 mm/s). Figs 6 and 7 show the typical analysis resulting from the use of 10 mm/s scanning speed and 600 W laser power.

The data generated during the solution procedure includes the depth of the 1325°C (1598 K) isotherms that approximately represent the fusion zone (FZ) boundary. These data were then used for comparison with experimental results. Fig. 8 shows a micrograph of the cross section of the deposits obtained for a laser power of 600 W and 10 mm/s scanning speed. From such a micrograph, the depth and width of the FZ was measured. Just as those line builds are physically sectioned, a section through the centerline of the model was taken. ANSYS model predictions of the FZ were superimposed on this micrograph. The isotherms corresponding to the FZ boundaries calculated by analytical model (Equations 13 and 22) are also superimposed on the micrograph. These isotherms represent the positions that were heated to a maximum temperature of 1325°C.

The model was also run for the other laser powers and scanning speeds. The temperature of each nodal point within the solid was calculated as a function of time. For each laser power and scanning speed, the maximum depth and diameter of the 1325°C temperature contours were measured. These measurements are plotted in Fig. 9, and they may be compared directly with the experimental measurements of the FZ dimensions as well as with the results obtained by analytical model (Equation 22).

The isotherms corresponding to the 1325°C, calculated both by numerical and analytical models, are also superimposed on the images of the molten pool acquired on-line by a laser-strobe vision system (Fig. 10). The isotherms show agreement between the simulated results and the results obtained by an image processing algorithm developed in [17] for validation. Furthermore, the results are validated for other processing parameters as well (scanning speed, laser power). The size and shape of the molten region obtained on-line is almost the same as those obtained by simulation for all applied laser powers and scanning speeds. In addition, by observing the molten pool it can be seen that the pool

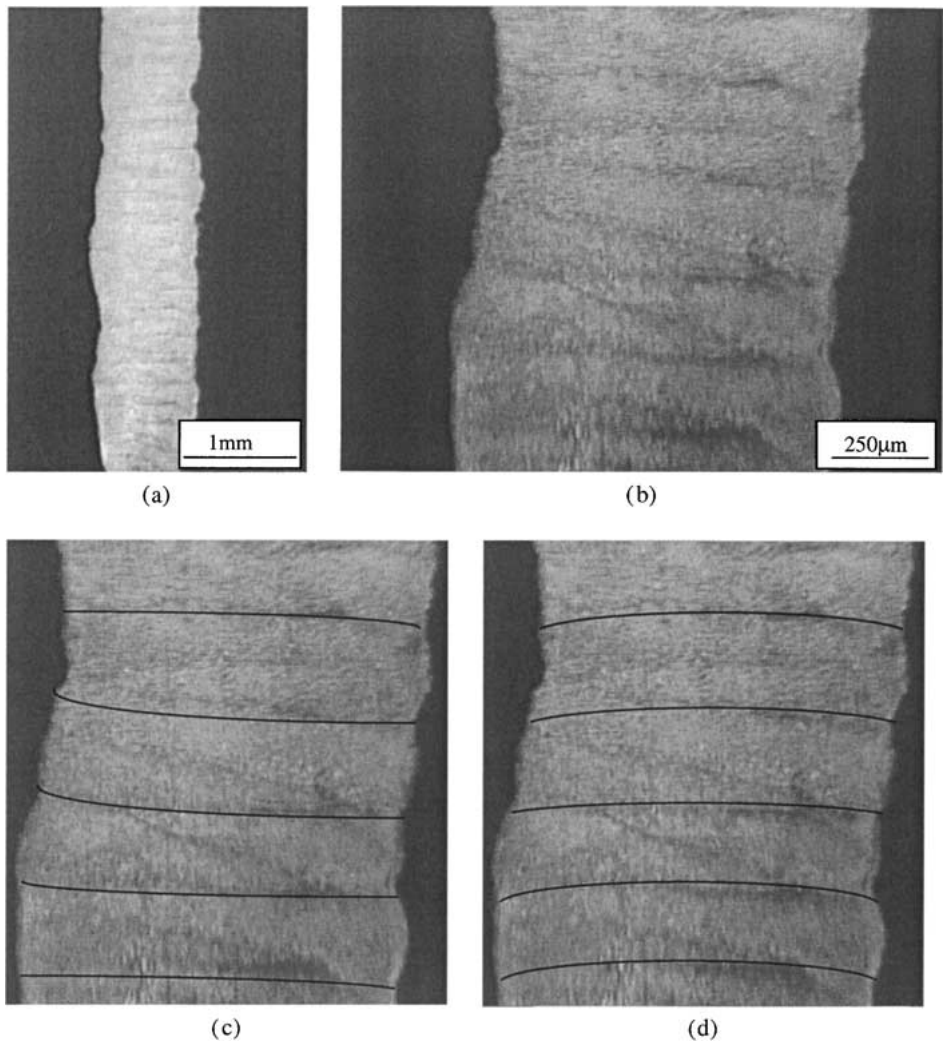

Figure 8 Micrograph of the cross section of the direct laser metal powder deposition showing model predictions of the fusion zone boundaries: (a) 8×, (b) 32×, (c) the numerical modeling, and (d) the analytical modeling.

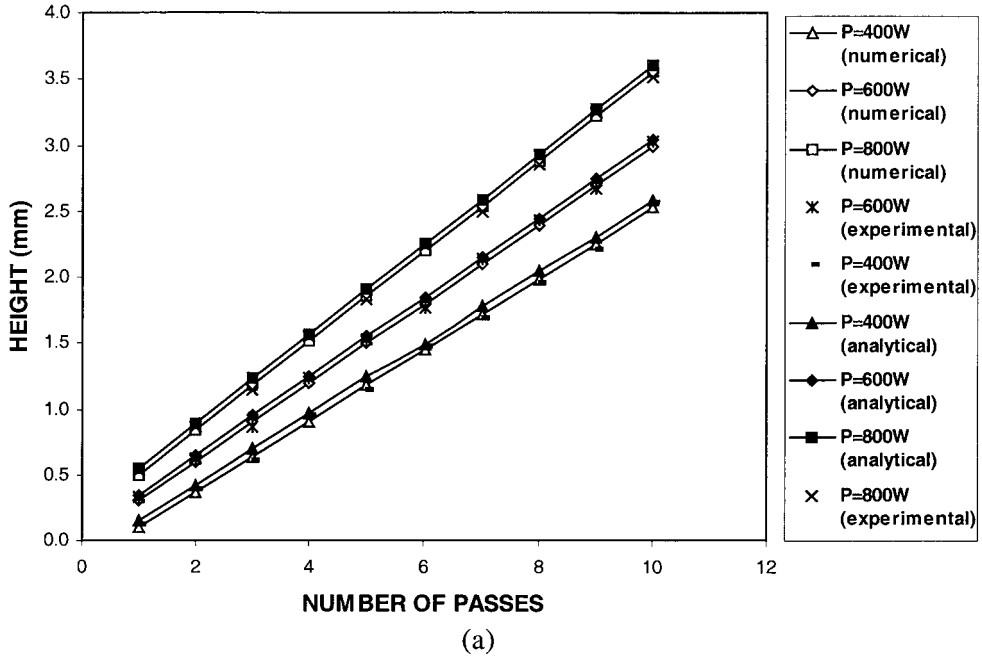

(a)

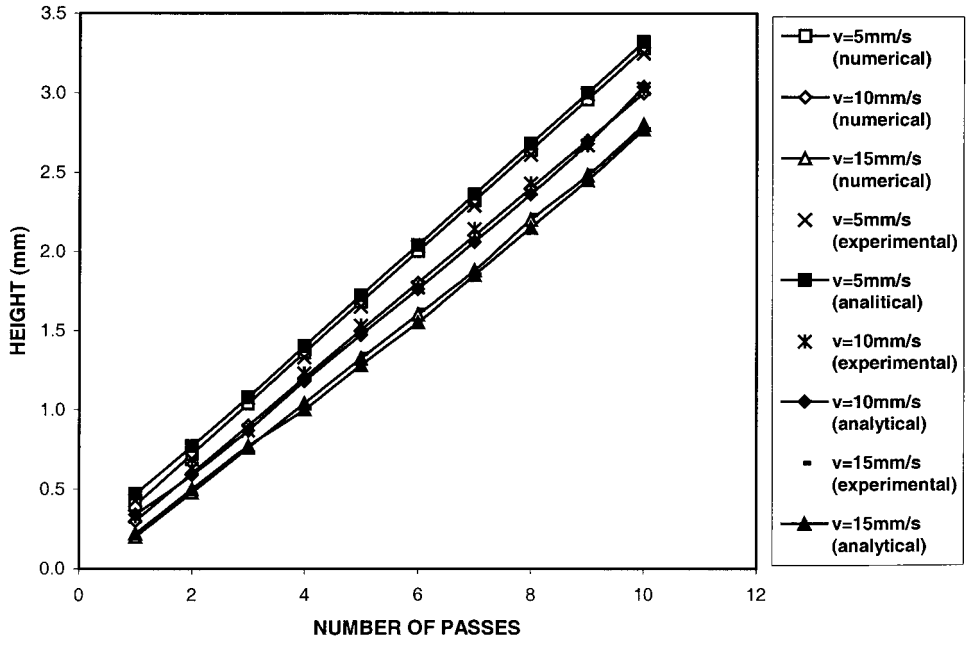

(b)

Figure 9 FZ depths compared with model predictions for different: (a) laser powers and (b) scanning speeds.

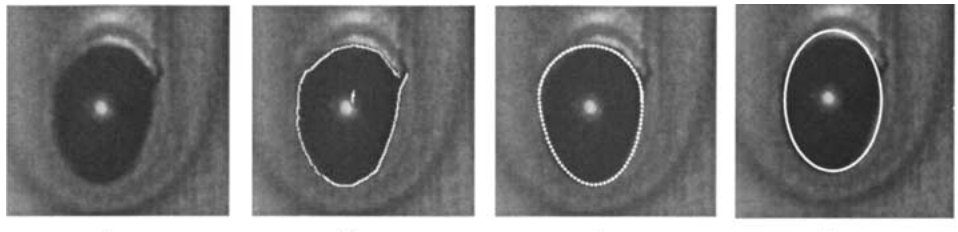

Figure 10 Comparison of the FZ boundaries obtained by the processing results of the edge detector with those obtained by the modeling: (a) original image acquired by high shutter-speed camera, (b) processing result of edge detector, (c) numerical modeling result, and (d) analytical modeling result.

is deeper at the end than on the front because of the heat accumulation. However, an increase of the laser power and decrease of the scanning speed results in a wider molten pool. The display of these distinct characteristic signatures on the surface temperature patterns allows one to estimate the depth of the molten pool, which is the major issue of the recent trend toward surface modification automation. The obtained results can be used for molten pool depth estimation and close-loop control of direct laser metal powder deposition process,

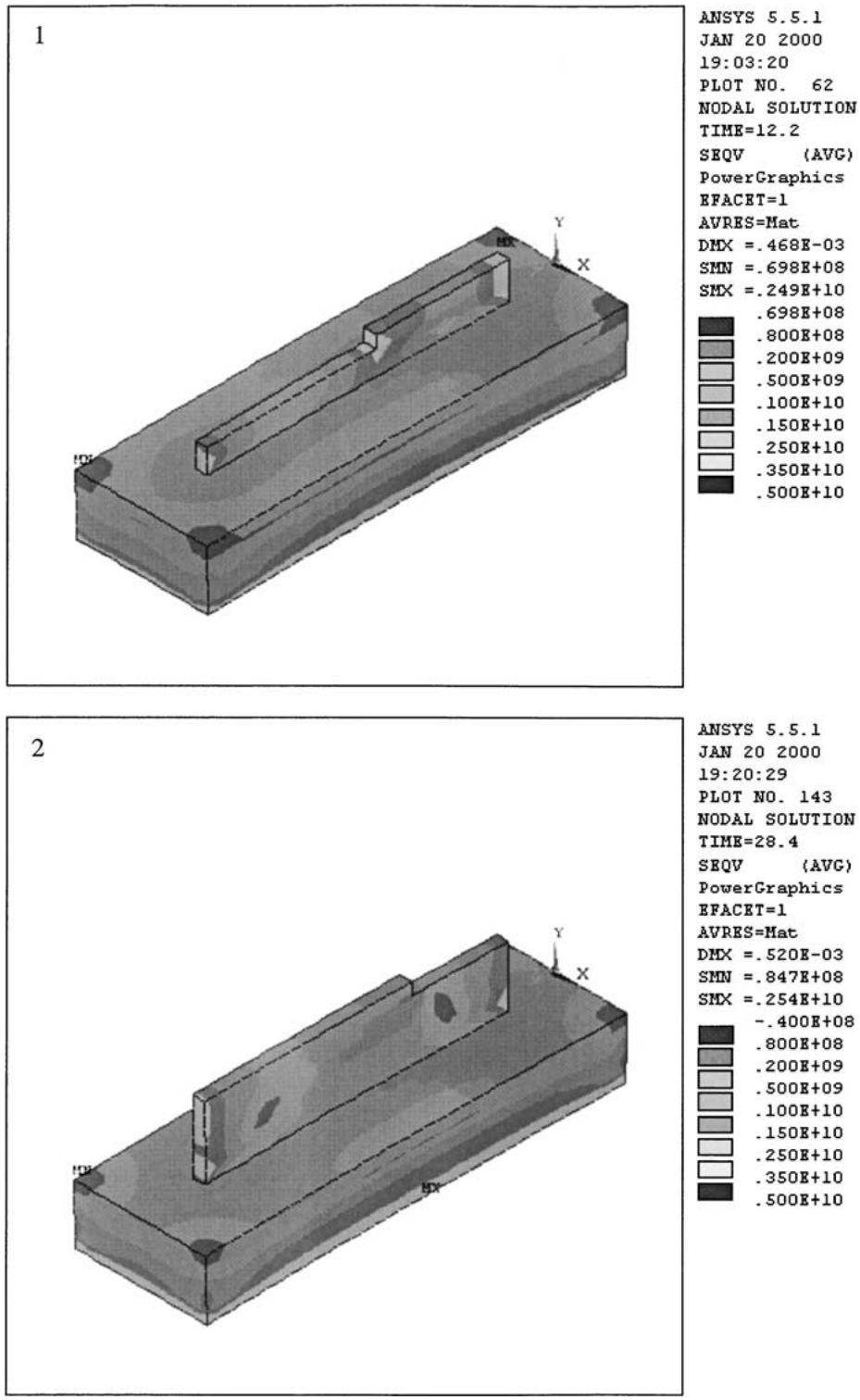

Figure 11 Distribution of residual stresses during direct laser metal powder deposition (laser power: 600 W, scanning speed: 10 mm/s): (1) $\tau = 12.2$ s and (2) $\tau = 28.4$ s.

combined with reliable sensors presently available for the remote real-time measurement of the absolute molten pool temperature [1]. This will our objective in subsequent research.

7.2. The analysis of residual stresses

The distribution of residual stresses obtained by finite element modeling resulting from the use of 10 mm/s scanning speed and 600 W laser power are shown in Figs 11 and 12.

Residual stresses were also investigated with the x-ray diffraction technique. X-ray residual stress calculations were undertaken perpendicular to the direction of the line builds using the $\sin^2 \psi$ method [18]. The technique is not described here in detail as the theoretical background and basic principles have been recently summarized [19]. The distribution of residual stresses within a single layer obtained by finite element modeling was compared with that obtained by x-ray diffraction technique showing satisfactory agreement (Fig. 13). The figure indicates that there is a strong

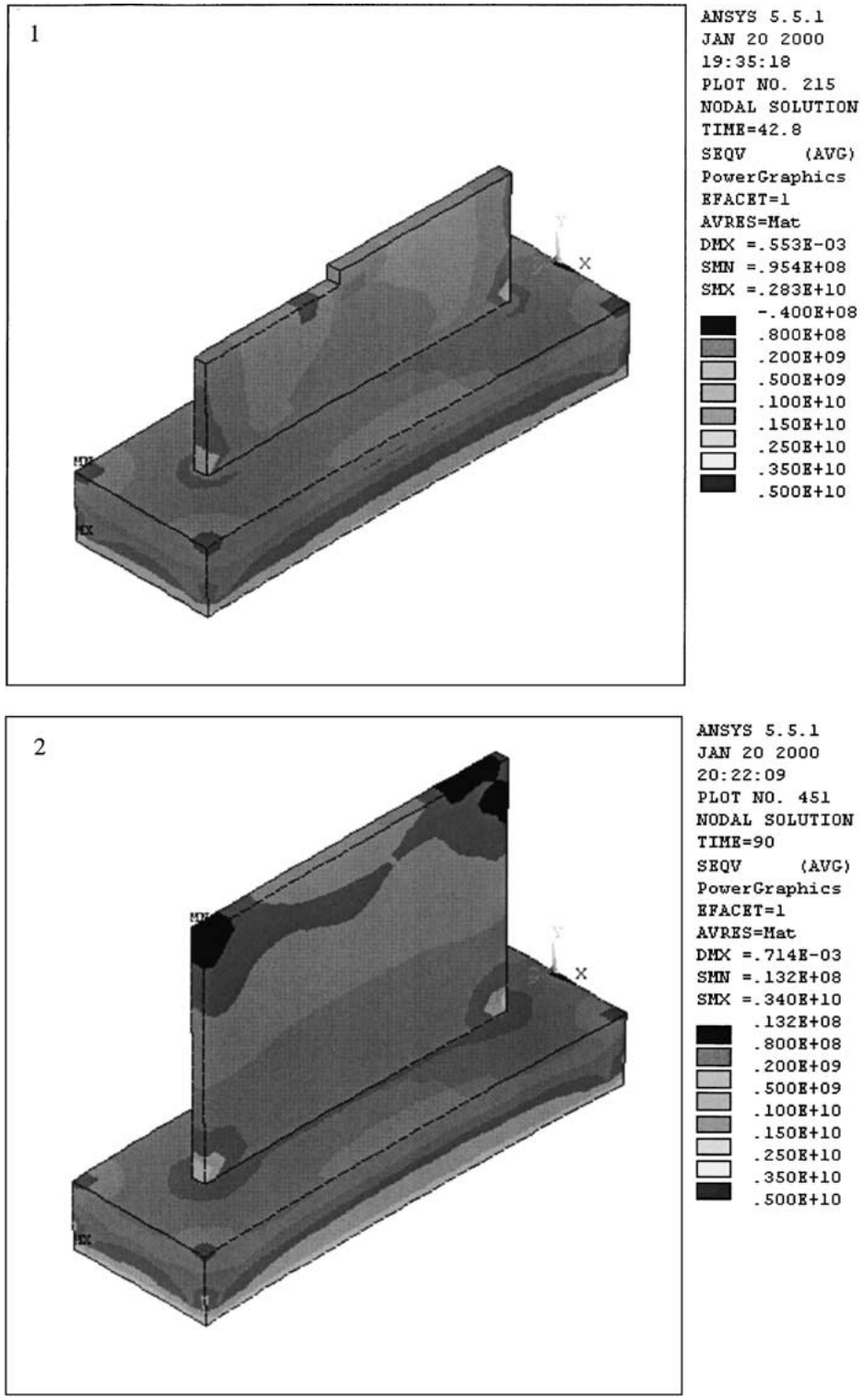

Figure 12 Distribution of residual stresses during a direct laser metal powder deposition (laser power: 600 W, scanning speed: 10 mm/s): (1) $\tau = 42.8$ s and (2) $\tau = 90$ s.

variation in the level of residual stresses inside the deposited layers. The distribution of residual stresses is tensile within the center of the layers and compressive towards the edges. Moreover, immediately outside the melt-pool the stress in the heat-affected zone is tensile. It can be expected that this will revert to compressive stress as the distance from the melt track increases. However, due to the time-consuming nature of x-ray diffraction technique, this detail was not measured, but is confirmed by the finite element modeling (please see Figs 11 and 12).

The effect of subsequent layers deposition on the residual stresses distribution is shown in Fig. 14. The sample was allowed to cool below 50°C between each subsequent build in order to eliminate any preheating effect. The data presented in Fig. 14 indicate a distribution of stresses within the first layer (left) similar to that plotted in Fig. 13. However, there is a progressive increase in the level of tensile residual stresses as subsequent layers are deposited. In addition, in the case of subsequent layers deposition, transverse cracks (i.e. perpendicular to the direction of laser scan (Fig. 15)) as

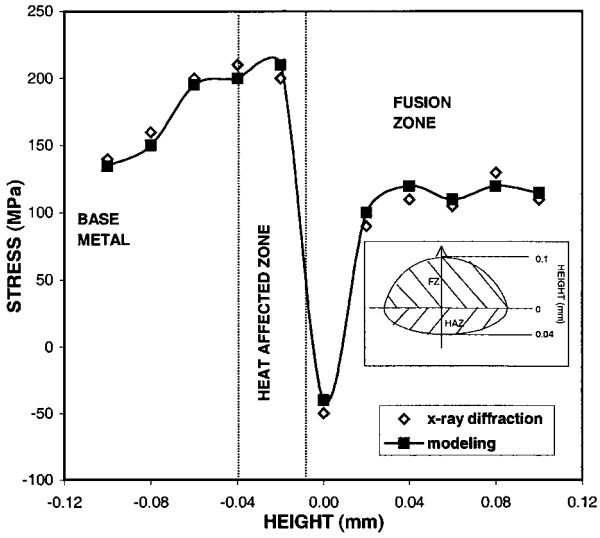

Figure 13 Distribution of residual stresses within a single layer-comparison of the results obtained by x-ray diffraction method with those obtained by the modeling (laser power: 600 W, scanning speed: 10 mm/s).

well as longitudinal cracks (i.e. parallel to the direction of laser scan (Fig. 16)), were detected. This can be explained by a stepwise increase in the residual stresses with each successive, overlapping laser track [19]. We deliberately designed experiments in which each subsequent deposited layer was allowed to cool below 50°C before carrying out the following pass. This was to avoid the effect of preheating on the residual stresses. However, cracking can be avoided by preheating the specimen, but also reduces the cooling rate. The mechanism that prevents cracking by preheating increases the ductility of the MONEL 400-alloy.

The effect of a preheating treatment to 400°C and post-heat treatment to 600°C for 1 hour is shown in Figs 17 and 18, respectively. When preheated to 400°C, the residual stresses are reduced to about +400 MPa. After a stress-relieving treatment at 600°C, the residual tensile stresses are further reduced to about +200 MPa. These results suggest that shrinkage in the melt-zone produces residual tensile stresses and that stress-relieving could reduce those values.

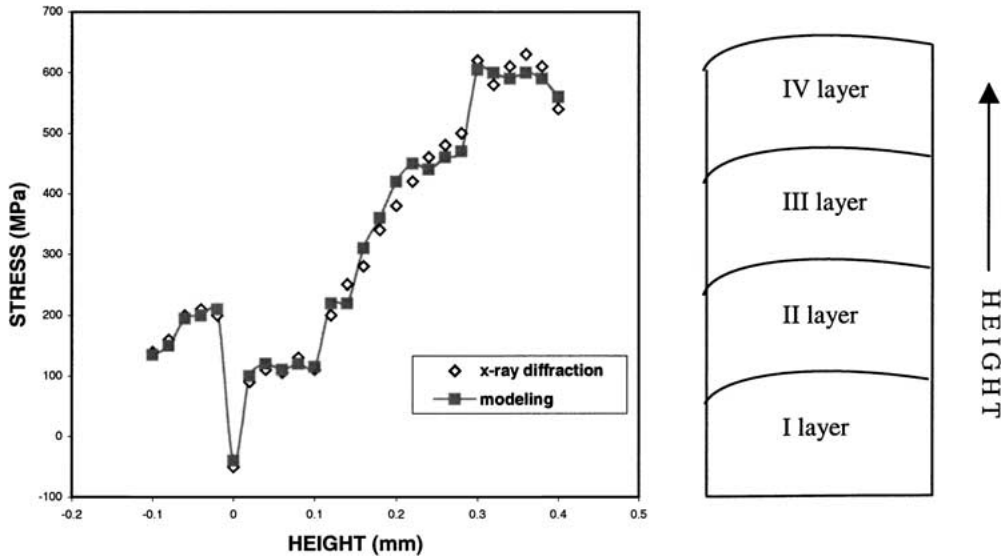

Figure 14 Distribution of residual stresses within subsequent layers-comparison of the results obtained by x-ray diffraction method with those obtained by the modeling (laser power: 600 W, scanning speed: 10 mm/s).

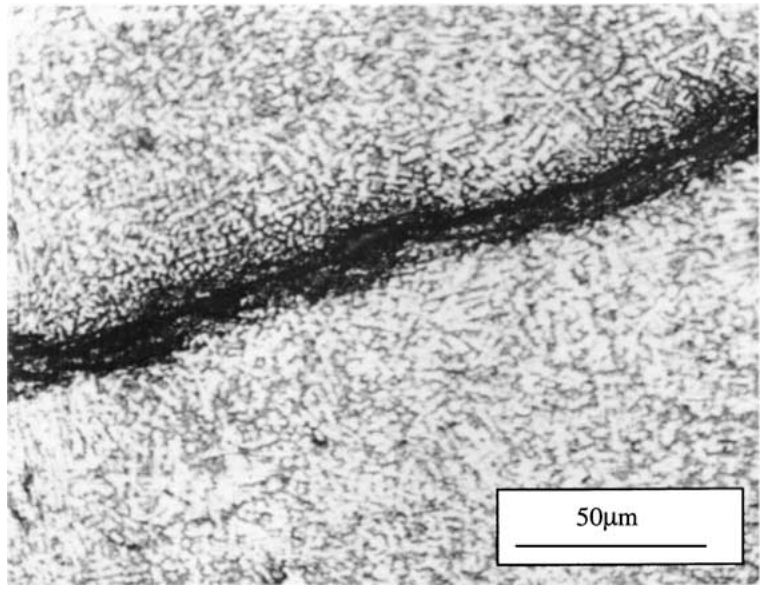

Figure 15 Micrograph showing typical perpendicular crack formation associated with a single layer build (500×).

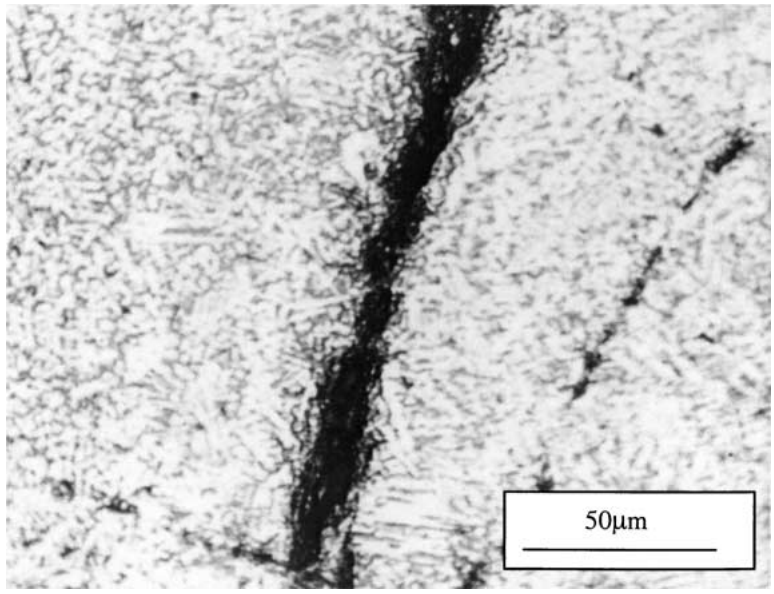

Figure 16 Micrograph showing typical longitudinal crack formation associated with the subsequent layers builds (500×).

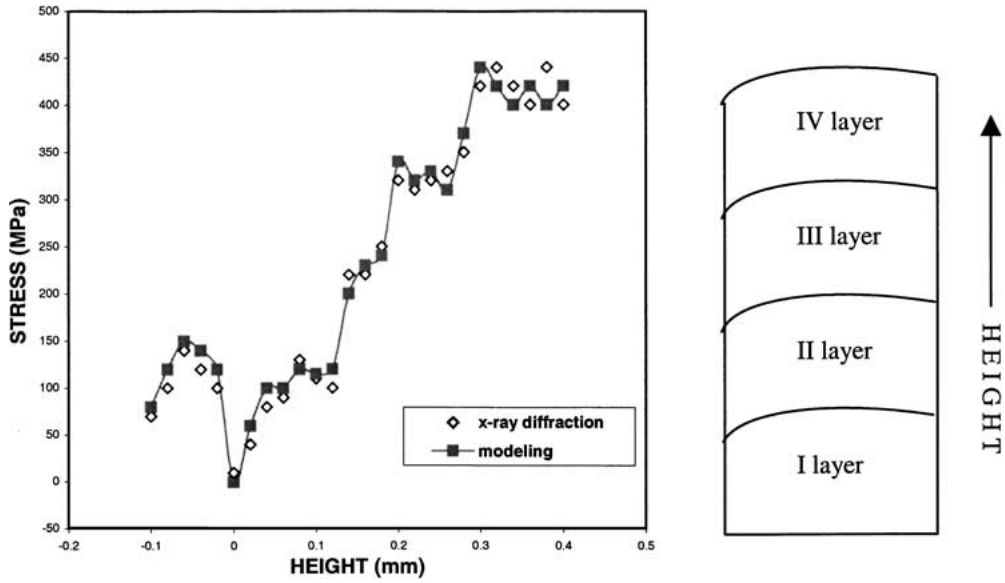

Figure 17 Distribution of residual stresses within the subsequent layers builds preheated to 400°C—comparison of the results obtained by the x-ray diffraction method with those obtained by the model.

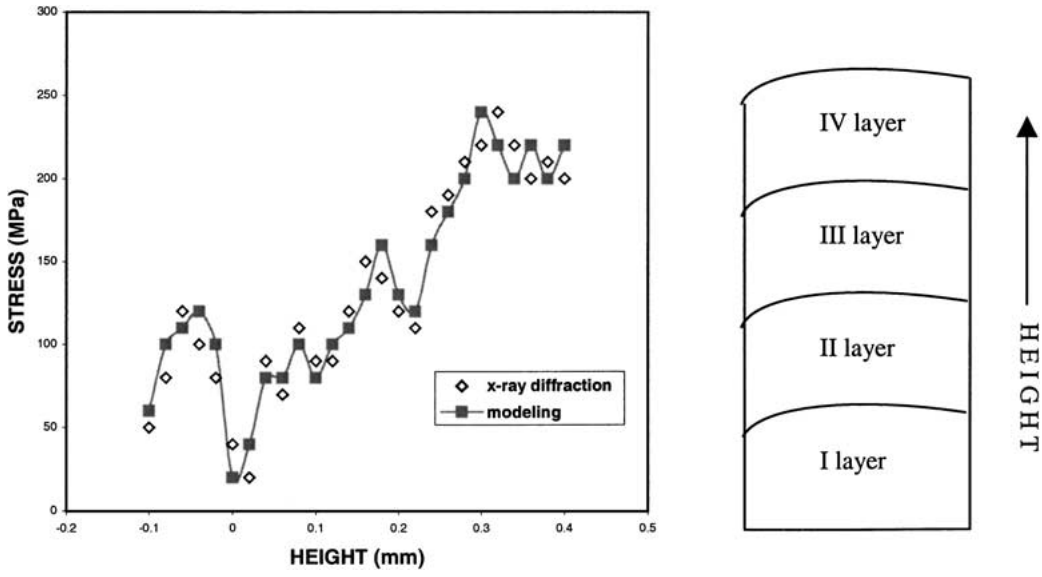

Figure 18 Distribution of residual stresses within the subsequent layers builds after the post heat treatment to 600°C for 1 h—comparison of the results obtained by the x-ray diffraction method with those obtained by the model.

8. Conclusion

A three-dimensional model of the heat flow and residual stresses in a direct laser metal powder deposition process has been developed. Both numerical and analytical models are addressed. The simulation and experimental results are in good agreement.

The simulation results provide the cross-sectional shape of the molten pool. In addition, these results are certified by the topside image of the molten pool acquired on-line by the high-shutter-speed camera. The pool is deeper at the end than at the beginning of the bead because of the heat accumulation. In reality, this means there are relations between the shape and the depth of the molten pool. Therefore, a capability of computationally predicting the fusion zone boundary allows the possibility of constructing a direct laser powder deposition monitoring system based on temperature-sensing and machine vision.

Modeling results of residual stress calculations are confirmed by x-ray diffraction residual stress measurements. In comparison with a single layer build, subsequent layer builds result in an increase in the residual stresses. This data can be used to rationalize the observation that cracking may occur in a longitudinal, as well as transversal, direction. More importantly, cracking can be avoided by preheating the specimen. The cracking can also be avoided by stress relieving which significantly reduces the residual tensile stress level.

Finite element modeling has been able to computationally predict various deviations from ideal conditions providing information that is necessary for engineering applications.

Acknowledgment

This work was financially supported by the U.S. Department of Education's Grant P200A80806-98.

References

1. W. HOFMEISTER *et al.*, *JOM* **51** (1999) 274.
2. H. S. CARSLAW and J. C. JAEGER, in "Conduction of Heat in Solids" (Clarendon Press, Oxford, UK, 1959) p. 134.
3. V. A. VINOKUROV, in "Welding Stresses and Distortion" (Boston Spa, London, 1987) p. 118.
4. D. RADAJ, in "Heat Effects of Welding; Temperature Field, Residual Stress, Distortion" (Springer-Verlag, Berlin, 1992) p. 1.
5. A. BOYCE, P. H. MORTEN and T. BELL, in "Metals Handbook, Vol. 5" (ASM International, Materials Park, OH, 1994) p. 835.
6. Y. NAMBA, in Proceedings of the Conference on Laser Forming in Space, Osaka, Japan, April 1986, edited by C. P. Wang, p. 403.
7. M. R. FREWIN and D. A. SCOTT, *Welding Journal* **78** (1999) 15.
8. S. BROWN and H. SONG, *J. Eng. Ind.* **114** (1992) 441.
9. J. LI, J. MERLIN, J. CHEN and Z. FAN, *Chinese Journal of Laser* **3** (1997) 280.
10. M. BASS, in Proceedings of the Conference on Laser-Materials Interactions, San Diego, July 1988, edited by T. Brown (Academic Press, New York, 1998) p. 122.
11. J. A. GREENWOOD, W*ear* **150** (1991) 153.
12. R. B. KUILBOER, P. K. KIRNER, J. MEIER, M. RUND and M. F. SCHNEIDER, in "Annals of the CIRP" (Wiley, London, 1990) p. 585.
13. F. P. INCROPERA and D. P. DE WITT, in "Fundamentals of Heat and Mass Transfer" (Wiley, Chichester, 1974) p. 120.
14. M. F. SCHNEIDER, in Ph. D. thesis, University of Twente, Enschede, Netherlands, 1998, p. 104.
15. ANSYS Theory Manual, Release 6.0 (ANSYS Inc., USA, June 2001).
16. C. S. KIM, in Technical Report ANL-75-55, Argonne National Laboratory, Argonne, 1975, p. 1.
17. D. HU, M. LABUDOVIC and R. KOVACEVIC, in Proceedings of the 9th International Conference on Computer Technology in Welding, Detroit, Michigan, September 1999 NIST Special Publication 949 (NIST, 2000) p. 417.
18. A. B. KLOSTERMAN and J. T. M. DE HOSSON, in Proceedings of the International Conference on Computer Methods and Experimental Measurements for Surface Treatment Effects, Milan, Italy, July 1995, edited by G. Brown (Academic Press, New York, 1995) p. 247.
19. M. R. JAMES and J. B. COHEN, in "Experimental Methods in Materials Science" (Academic Press, New York, 1958) p. 30.

Received 21 February
and accepted 26 August 2002